

Out-of-time-order Correlators and Chaos in Quantum Billiards

Tasnim Anzum Ador, Nayeem Farid, and Tibra Ali

*Department of Mathematics and Natural Sciences, School of Data and Sciences,
Brac University, Dhaka 1212, Bangladesh.*

*E-mail: tasnim.anzum@bracu.ac.bd, nayeemfarid919@gmail.com,
tibra.ali@bracu.ac.bd*

ABSTRACT: We examine three billiard systems – the cardioid, diamond (Superman), and Sinai billiards – all of which are known to be classically chaotic. We compute their classical Lyapunov exponents, and using out-of-time-order correlators (OTOCs) in the semi-classical regime, we also derive their quantum Lyapunov exponents. We observe that the classical and quantum Lyapunov exponents are in agreement, strengthening the role of OTOCs as a diagnostic for quantum chaos in billiard systems. At very low temperatures, the OTOC of the Sinai billiard shows sharp growth, a phenomenon absent in the other two billiards. We identify the source of this anomalous behaviour in the geometry of the ground state wave function of the Sinai billiard, which is more sensitive to the curvature of the billiard compared to the other billiards. We also remark on the late-time behaviour of the OTOCs and how the scrambling/Ehrenfest time is related to the temperature of quantum billiards.

KEYWORDS: OTOC, Chaos, Lyapunov Exponent, Ehrenfest Time

Dedicated to the memory of all the Bangladeshi students who were either martyred, maimed, or injured in the struggle to free their country from dictatorship.

Contents

1	Introduction and Overview	2
2	Review of Quantum Chaos and OTOC	3
2.1	Definition of OTOC	4
2.2	Connection between OTOC and classical chaos	5
3	Out-of-Time-Order Correlators for Billiard Systems	5
3.1	Formalism for OTOC computations	6
3.2	Time windows	7
4	The Three Billiards	9
4.1	Sinai billiard	9
4.2	Cardioid billiard	10
4.3	Diamond/Superman billiard	11
5	Numerical Calculation of Classical Lyapunov Exponents	12
5.1	Lyapunov exponents and hyperbolicity	12
5.2	Classical Lyapunov exponents of the three billiards	13
6	Numerical calculation of OTOCs	15
6.1	OTOCs and Wavefunctions	15
6.2	Asymptotic Nature of OTOC at Large Times	20
7	Quantum Lyapunov Exponents and Thermal OTOCs	20
8	Temperature Dependence of Ehrenfest Times	25
9	Discussion	28
A	Assessment of the error resulting from level truncation	30
B	Averaging Collision Distance to Scale Length Parameters	31

1 Introduction and Overview

Originally introduced as a way of examining the semi-classical behaviour of superconductors by Larkin and Ovchinnikov more than five decades ago [1], the out-of-time-order correlator (OTOC) has featured prominently in the exploration of quantum chaos in recent years. In its recent renaissance, it has received significant attention initially motivated by the holographic description of black hole physics [2–6]. OTOCs have been useful in capturing chaotic behaviour in a wide array of quantum systems such as the SYK model [4], the kicked rotor [7], spin chains [8], and quantum billiards [7, 9, 10], to name a few.

In general, OTOCs represent the growth of Heisenberg operators and measure the way quantum information spreads and gets scrambled over time [11]. The Lyapunov exponent, on the other hand, is an important quantity in classical chaos that measures the time scale (via the Lyapunov time) over which predictability breaks down. In many quantum systems there exist semiclassical regimes in which the growth of the OTOC has a similar exponential growth region and a “quantum” Lyapunov exponent [4] can be identified. In [6], Maldacena, Shenker and Stanford conjectured, from general grounds, that the quantum Lyapunov exponent is bounded from above by the temperature of the system. Black holes, believed to be nature’s fastest scramblers, saturate this bound. Other systems that saturate the bound include the SYK model which has a holographic description in terms of black holes.

Chaotic billiards are some of the simplest examples of classically chaotic systems. On general grounds one expects their quantum counterparts to exhibit chaos in the semiclassical limit: Ehrenfest’s theorem guarantees chaotic dynamics in the quantum versions of chaotic billiards well before Ehrenfest time. But some of the first attempts to identify an exponential region and derive a Lyapunov exponent from the quantum stadium billiard proved to be difficult [9]. However, Jalabert et. al. [10] were able to develop a method for dealing with the semiclassical limit of low-dimensional systems and they identified a region in which the thermal OTOC exhibits exponential growth. Therefore it was possible to derive a quantum Lyapunov exponent for the quarter stadium billiard. (For a review of their method and the role of OTOC in quantum chaos in general see [12].) Rozenbaum et. al. [13] introduced a state-independent way of characterizing quantum chaos by studying the level statistics of a new class of “Lyapunovian” operators. Based on this, they were able to derive the Lyapunov exponent using a non-thermal OTOC.

In this paper, building on the methods of [9, 10, 12, 13], we examine three billiard systems, other than the stadium billiard, which are known to be classically chaotic: the cardioid, diamond, and Sinai billiards. While there are many different methods for approaching quantum versions of classically chaotic systems, our

motivation in this paper is to utilize the new and emerging tool of OTOC to derive the Lyapunov exponents of the simplest chaotic systems. We compute the quantum Lyapunov exponents using the semi-classical expansion of the OTOCs¹. We also compute the classical Lyapunov exponents to compare them to their quantum counterparts. For the Sinai and cardioid billiards, the quantum Lyapunov exponents agree well with their classical counterparts, but the agreement for the case of the diamond billiard is not as good. We rechristen the diamond billiard as the Superman billiard as its shape reminds us of the comic book hero's logo.

We also find that while at low temperatures the OTOCs do not have sharp growths in general, the Sinai billiard is an exception. By examining the *micro-canonical* OTOCs, we show that the origin of this anomalous behaviour lies in the geometry of the ground state wave function of the Sinai billiard which is sensitive to the curvature of the billiard in contrast to the ground states of the other two billiards under study.

Lastly, we give a couple of heuristic arguments as to why the Ehrenfest time t_E (*i.e.*, the scrambling time t^*) of chaotic billiards should have $1/\sqrt{T}$ dependence on the temperature.

Outline:

The outline of the paper is as follows. In Section 2, we introduce the OTOC and explain its connection to the quantum Lyapunov exponent in the semi-classical limit. This is followed in Section 3 by fundamental concepts from quantum chaos that we shall be using for computation. We then present, in Section 4, a review of the three classical billiards which we shall be studying. We use the cardioid billiard as an example for demonstrating some of the fundamental concepts. In Section 5, we compute the classical Lyapunov exponents of these billiards. In Section 6, we present the numerical calculations of the OTOCs and we examine the ground states of the three billiards. In Section 7 we calculate the quantum Lyapunov exponents and compare them with our classical computation, and in Section 8 comment on the temperature dependence of the Ehrenfest time. We conclude our paper with some observations in Section 9.

2 Review of Quantum Chaos and OTOC

The *Lyapunov exponent* is an important measure of chaos in classical systems. Let us consider a system with a one-dimensional phase space x . Two states of this system, starting from initial points x_0 and $x_0 + \delta x(0)$, evolve with time. Here $\delta x(0)$ is very small, and it is the separation of the two states at time $t = 0$. For a

¹We are grateful to the authors of [10, 12] for explaining details of their calculation.

chaotic system, this separation increases exponentially with time,

$$\delta x(t) \approx e^{\lambda t} \delta x(0) \quad (2.1)$$

where $\delta x(t)$ is the separation of the two states at time t , and λ , a positive, real constant, is the *Lyapunov characteristic exponent*, or the Lyapunov exponent for short. When considering a chaotic system with a multidimensional phase space, one can associate a Lyapunov exponent with each direction of phase space.

In the study of quantum chaos, however, the Lyapunov exponent may not seem like a useful or even a measurable quantity at first. This is because for quantum systems the notions of trajectories and phase spaces are not generally well-defined concepts. But using out-of-time-order correlators (OTOCs) [1], one *can* extract in many cases the Lyapunov exponent of quantum chaotic systems and compare them to their classical exponents. As mentioned in the introduction, OTOCs have captured significant attention recently due to their relevance in studying the relationship between black-hole horizon geometry and chaos [2, 3, 5]. Black holes were found to exhibit the same early exponential growth of OTOCs observed in classically chaotic systems, which led to terms such as “scrambling”, “quantum butterfly effect” and “quantum Lyapunov exponent”. This behaviour classifies black holes as fast scramblers, where information is quickly spread. Furthermore, Maldacena, Shenker, and Stanford [6] conjectured in 2016 that there is an upper limit to the OTOC growth rate, which is essentially determined by the temperature of the system. Explicitly, this bound is given by $\lambda \leq 4\pi k_B T / \hbar$.

The recognition of OTOCs and the quantum Lyapunov exponent in the arena of black holes and holography has led to their usefulness in quantifying quantum chaos in billiard systems which are known to be classically chaotic. Recently examinations of the stadium billiard [9, 10, 13] have paved the way for the application of these methods to other billiard systems which are known to be classically chaotic.

2.1 Definition of OTOC

The out-of-time-order correlator is defined as

$$C_T^{(AB)}(t) = \langle [B_t, A]^\dagger [B_t, A] \rangle. \quad (2.2)$$

In the above equation, A and B are Heisenberg operators (time-dependent operators), where the subscript t means that the respective operator has been time-evolved to time t with respect to the other operator. The angular brackets denote the thermal average of the quantity inside the brackets, which is calculated as $\langle \mathcal{O} \rangle \equiv \text{Tr}[\rho \mathcal{O}]$ for an operator \mathcal{O} in the canonical ensemble. Here, $\rho = Z^{-1} e^{-\beta H}$, where Z is the partition function, and $\beta = 1/k_B T$, where k_B is the Boltzmann constant and T is the temperature of the system. It is also possible to consider

temperature-independent OTOCs as was done in [13], but in this paper we restrict ourselves to thermal OTOCs (see Section 7).

Our goal is to use OTOCs to analyse the behaviour of measurable physical quantities in quantum systems. As these quantities are represented by Hermitian operators, we can limit our definition of the OTOC in Eq. (2.2) (which is valid for any two operators on the Hilbert space of the system) to the scenario where the operators A and B are Hermitian. The definition (2.2) then becomes

$$C_T(t) = -\langle [B_t, A]^2 \rangle \quad (2.3)$$

where T refers to the temperature of the system. For the sake of notational clarity we shall drop the superscripts as it will be obvious from the context which operators are involved in a particular OTOC. In quantum systems the growth of the OTOC is linked to the diffusion of quantum information known as information scrambling [11].

2.2 Connection between OTOC and classical chaos

When studying the behaviour of an OTOC in the context of the classical limit, it is possible to utilize the quasi-classical limit of $\hbar \rightarrow 0$, as was originally noted when introducing the OTOC [1]. In this limit, we can replace the commutator of two operators with the Poisson bracket of the corresponding classical quantities,

$$\lim_{\hbar \rightarrow 0} \frac{1}{i\hbar} [B, A] \rightarrow \{B, A\}. \quad (2.4)$$

By selecting the position and momentum operators, $B = x$ and $A = p_x$, and utilizing the quasi-classical limit, we get

$$\lim_{\hbar \rightarrow 0} [x_t, p_x] \rightarrow i\hbar \{x(t), p_x(0)\} = i\hbar \frac{\partial x(t)}{\partial x(0)}. \quad (2.5)$$

In the case of a fully classically chaotic system, we have $\partial x(t)/\partial x(0) \sim \exp(\lambda t)$, denoting the exponential sensitivity to initial conditions. Thus, the OTOC in the quasi-classical limit is given by

$$C_T^{\text{qc}}(t) \sim \hbar^2 \exp(2\lambda t). \quad (2.6)$$

The above equation is noteworthy, as it relates the OTOC (a quantum entity) on the left-hand side, to the Lyapunov exponent (a classical characteristic) on the right-hand side. Thus, it links the classical and quantum counterparts of a system.

3 Out-of-Time-Order Correlators for Billiard Systems

Units for the rest of this paper

Going forward, we adopt the units: $\hbar = k_B = 2m = 1$, where m denotes the mass of the particle. We consistently set the area of the billiard to $A = 1$.

3.1 Formalism for OTOC computations

Let H be a time-independent Hamiltonian where $H = H(x_1, \dots, x_n, p_1, \dots, p_n)$. As in [9] with the choice of $B_t = x(t)$ and $A = p(0)$ as operators, the OTOC in eq. (2.3) becomes:

$$C_T(t) = -\langle [x(t), p(0)]^2 \rangle. \quad (3.1)$$

In the following, we will leave out the argument of Heisenberg operators when $t = 0$ and denote them as $\mathcal{O} \equiv \mathcal{O}(0)$. We reformulate the OTOC in the basis of energy eigenstates of H :

$$C_T(t) = \frac{1}{Z} \sum_n e^{-\beta E_n} c_n(t), \quad c_n(t) \equiv \langle n | [x(t), p]^2 | n \rangle, \quad (3.2)$$

where $H |n\rangle = E_n |n\rangle$. The OTOC associated with a specific energy eigenstate, $c_n(t)$, will be called a *microcanonical OTOC*. $C_T(t)$ will be referred to as a *thermal OTOC* [9].

With the aid of the completeness relation, a microcanonical OTOC can be expressed as

$$c_n(t) = \sum_m b_{nm}(t) b_{nm}^*(t), \quad b_{nm} \equiv -i \langle n | [x(t), p(0)] | m \rangle \quad (3.3)$$

$b_{nm}(t)$ is Hermitian: $b_{nm}(t) = b_{mn}^*(t)$. We substitute $x(t) = e^{iHt} x e^{-iHt}$ and use the completeness relation again to write $b_{nm}(t)$ as

$$b_{nm}(t) = -i \sum_k \left(e^{iE_{nk}t} x_{nk} p_{km} - e^{iE_{km}t} p_{nk} x_{km} \right), \quad (3.4)$$

where $E_{nm} \equiv E_n - E_m$, $x_{nm} \equiv \langle n | x | m \rangle$, and $p_{nm} \equiv \langle n | p | m \rangle$.

The expression in (3.4) contains matrix components of p , which are not ideal because numerical derivatives of wave functions can lose accuracy. For a Hamiltonian of the form

$$H = \sum_{i=1}^N p_i^2 + U(x_1, \dots, x_N), \quad (3.5)$$

p_{nm} can be calculated using x_{nm} . We apply $\langle m | \dots | n \rangle$ to both sides of $[H, x] = -2ip$, and obtain

$$p_{mn} = \frac{i}{2} E_{mn} x_{mn}. \quad (3.6)$$

Substituting Eq. (3.6) into Eq. (3.4), we get

$$b_{nm}(t) = \frac{1}{2} \sum_k x_{nk} x_{km} \left(E_{km} e^{iE_{nk}t} - E_{nk} e^{iE_{km}t} \right). \quad (3.7)$$

Once we know the matrix elements of x and the energy spectrum E_n , OTOCs can be computed using Eqs.(3.2), (3.3), and (3.7). However, in actual numerical calculations a sufficiently large cut-off for the number of energy eigenvalues and eigenstates considered must be chosen. For the circle and stadium billiards the OTOCs were calculated in ref. [9].

3.2 Time windows

The quasi-classical form (2.6) of the OTOC suggests that classical properties can emerge in quantum systems. However, this behaviour is only present in a specific type of system and within a particular time-frame as discussed in [12, 14]. (Also see [6] which discusses the hierarchies of different time-frames.) Therefore, it is essential to understand the various time-frames that can be observed in the evolution of the OTOC. Many previous studies on the time evolution of various systems have shown that the OTOC can generally be classified into three different time-windows, as illustrated in Fig. 1.

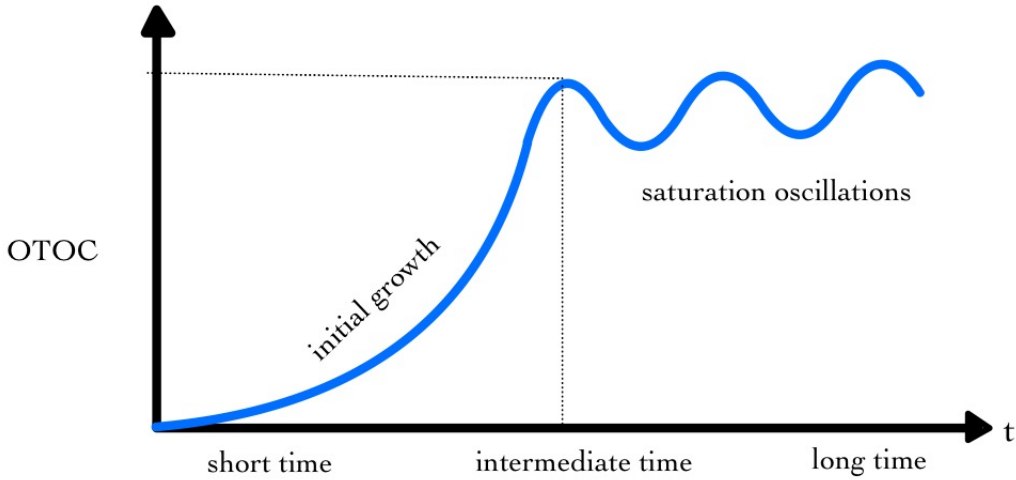


Figure 1: A blueprint for the time-windows of the OTOC. If the system is chaotic, it is anticipated that the initial growth will be exponential. The growth may take on other shapes if the system is not chaotic. The OTOC will stabilize and exhibit oscillations around a constant value after the scrambling time t^* . In the chaotic cases, the oscillations are highly suppressed, and the OTOC progresses toward an almost constant value. The figure shown here is a replica of a figure in [12].

Short times

The short-time window signifies the start of the process where the influence of the time-dependent Heisenberg operator expands, driven by the dynamics of the Hamiltonian. Using the BCH formula, at the beginning, the OTOC is predicted to increase following a power law. Following this initial stage, the OTOC will continue to increase steadily for a brief period before reaching scrambling time t^* . This behaviour has been extensively analyzed for short times, and predictions such as Eq. (2.6) have been made.

In [10], the authors developed a semi-classical approach to computing the OTOC of systems with low number of degrees-of-freedom based on earlier ideas

of semi-classical theory of chaos [15]. As a result they found a region of exponential increase of the OTOC characterized by a positive Lyapunov exponent. This behaviour emerges after a much faster growth during an extremely short time window. The time window for detecting the Lyapunov regime is temperature-dependent, with longer intervals observed at lower temperatures. See Section 8 for a discussion of the temperature dependence of the scrambling time.

Intermediate times

At around the scrambling time t^* , the initial growth stops, and the OTOC becomes relatively stable, maintaining an approximately constant value, with some minor fluctuations in certain cases. This time interval is commonly referred to as “intermediate times” and is particularly significant for highly chaotic systems, as it represents the duration between t^* and complete relaxation.

The scrambling time t^* marks the point at which information about the initial state becomes widely spread throughout the available space. For a single particle system with a bounded space and classical chaotic dynamics, this time corresponds to the Ehrenfest time t_E . The Ehrenfest time is defined as the time it takes for a narrow, coherent wave-packet to spread over whole system. It is given by $t_E = \lambda^{-1} \ln(a/\hbar)$ [6], where the constant a is determined by the system size and the initial wave-packet size.

Long times

One aspect of the OTOC in strongly chaotic systems is that after the scrambling time, the value of the OTOC becomes constant. It has been observed that the system’s dynamics greatly impact the long-time behaviour of the OTOC, whether it is chaotic or regular. Therefore, studying fluctuations in the long-time regime can provide a deeper understanding of the system’s behaviour.

For one-body systems with fully chaotic classical dynamics, the saturation value of the OTOC scales with the system size and temperature in a linear fashion when $B = X$ and $A = P_X$. However, the temperature scaling can differ for other operator choices. A study described in ref. [16] suggests that the integrability of the one-body dynamics and the complexity of the selected operators might alter the temperature scaling of the OTOC saturation value.

The long-time behaviour of the OTOC can provide accurate measures of quantum chaos, and analyzing its oscillations can quantify the shift from regular to chaotic dynamics. For non-chaotic systems, it is expected that OTOCs at long times will exhibit strong oscillations, whereas for strongly chaotic systems these oscillations are expected to be suppressed [12]. This method is consistent with other indicators of chaos commonly used [17].

4 The Three Billiards

We now introduce the three classically chaotic systems which are the main characters of our paper: the **Sinai**, **cardioid**, and **diamond** billiards. In the subsequent sections, we calculate the classical Lyapunov exponents of these systems and then move on to compute their OTOCs. This facilitates a comparison between classical and quantum dynamics. As mentioned in the introduction, our examination of the OTOCs of these billiards is done along the lines of the analyses of the stadium billiard carried out in [9, 10]. We will examine the growth rate of OTOC at low temperatures and its saturation behaviour at late time. The upper limit that we take for the temperature will be dictated by the existence of a semi-classical region which, as we shall see, starts to disappear at high temperatures. We will compare semiclassical results with numerical quantum calculations done on our selected billiards and connect these results with predicted limits on OTOC growth rate.

4.1 Sinai billiard

The Sinai billiard is based on the Lorentz gas system, proposed originally by Lorentz in 1905 as a model for the behaviour of a dilute electron gas in a metal. In this model, the electrons are assumed to interact with the fixed heavier atoms in a lattice but not with each other.

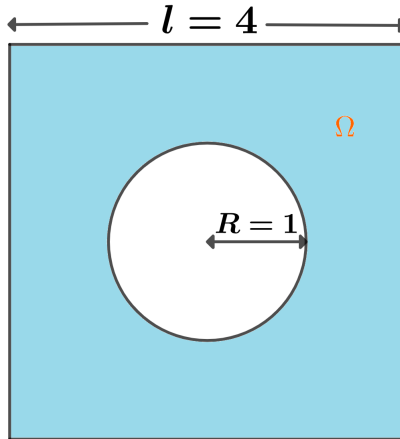


Figure 2: The Sinai billiard enclosure. The particle is confined within the shaded region Ω , and the deformation parameter is $\ell/R = 4$.

The Sinai billiard is a simplified version of this system consisting of a single hard disk placed at the centre of a square box [18]. The point-like particle moves freely within the region bounded by the box and the disk, and undergoes elastic reflections on the walls of this region. The deformation parameter is determined

by ℓ/R , where ℓ^2 is the area of the box and R is the radius of the disk. We fix the deformation parameter at $\ell/R = 4$ for our numerical calculation, as depicted in Fig. 2. The units of length used here are arbitrary. They are fixed by the requirement that the area $A = 1$.

The presence of a circular dispersing wall in Sinai billiards makes them chaotic for a finite deformation parameter ℓ/R . They are also ergodic but non-hyperbolic. However, if we consider only particle collisions with disks and no flat walls, these billiards are known to be hyperbolic and are called infinite horizon billiards [19]. In fact, any billiards with everywhere dispersing walls are chaotic and hyperbolic [20]. Our one-disk Sinai billiard exhibits the stickiness property due to the presence of flat walls. Roughly speaking, stickiness of a system is the propensity of some of its chaotic paths to spend considerable chunks of time very close to the non-chaotic regions of the phase space [21]. This property has an impact on the system’s dynamics, and as a result, accurately calculating the Lyapunov exponent is a challenging task.

4.2 Cardioid billiard

Our next classically chaotic billiard system of interest is the cardioid billiard. The cardioid billiard consists of a particle confined within a cardioid, which is a 2-dimensional “heart-like” shape, depicted in Fig. 3.

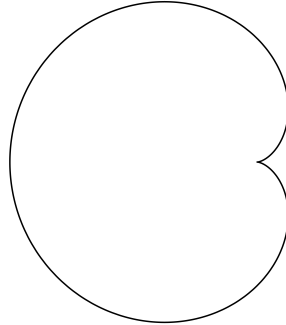


Figure 3: The cardioid shape

The cardioid billiard is part of the family of cos-billiards described by the parametric equation

$$r(\gamma) = 1 + \varepsilon \cos \gamma, \quad (4.1)$$

specifically for the deformation parameter $\varepsilon = 1$. Its boundary is made up entirely of focusing walls that intersect at a single point, forming a cusp. It has been proven that the cardioid billiard is both ergodic and mixing² [22–24].

²In ergodic motion, the trajectory successively fills the phase space. The nature of the movement during mixing is different. Initially, the system covers the whole space with a grid of trajectories for a particular duration of $t = T/2$. Then after a time $t = T$, the phenomenon is repeated,

4.3 Diamond/Superman billiard

The final billiard system we will be exploring in this paper is the diamond billiard. The diamond billiard is a classically chaotic system that is non-integrable, where a particle is confined within a two-dimensional enclosure that has a shape resembling a diamond or the outline of the logo of Superman. The enclosure is made up of a half-stadium combined with a triangular region at the bottom, as illustrated in Fig. 4.

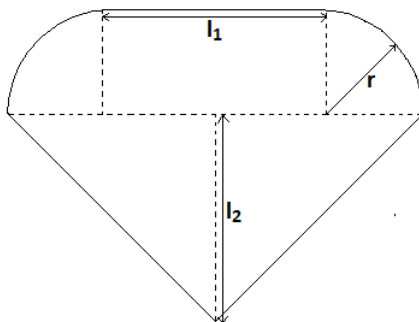


Figure 4: The diamond/Superman shape

We denote the radii of the two quarter-circles on each side of the shape by r , the length of the horizontal line making up the very top of the boundary of the enclosure by ℓ_1 , and the length of the vertical line bisecting the triangular region as ℓ_2 , as shown in Fig. 4. We shall define a deformation parameter σ in the same way as was done in ref. [25]. The relationships between σ and the quantities r , ℓ_1 and ℓ_2 are given below.

$$\begin{aligned} r(\sigma) &= 1 - \sigma \\ \ell_1(\sigma) &= \frac{5}{2} + \sigma \\ \ell_2(\sigma) &= \sqrt{\frac{3}{4}} \ell_1(\sigma) \end{aligned} \tag{4.2}$$

Thus, the value of σ determines the shape of the enclosure. It takes values in the range $0 \leq \sigma \leq 1$, and the shape changes from a diamond to an equilateral triangle as σ goes from 0 to 1. In our calculations, we took σ to be 0, thus giving us the diamond/Superman shape.

and the cell sizes of the grid are roughly halved. Mixing is more potent than ergodicity, meaning that the presence of mixing guarantees ergodicity, but the inverse is not necessarily true.

5 Numerical Calculation of Classical Lyapunov Exponents

5.1 Lyapunov exponents and hyperbolicity

Lyapunov exponents describe a system's sensitivity to initial conditions. The Lyapunov exponents associated with a specific point in the phase space determine how rapidly the nearby trajectories diverge with time. In billiard systems, particles move in a straight line between collisions. As a result, the trajectories diverge linearly between collisions. Thus, the chaotic dynamics of a billiard system are contained within its collisions. For this reason, we use the collision index n , which denotes the number of collisions, as the parameter to measure sensitivity to initial conditions instead of time [25, 26].

We consider a pair of particles that start out very close to one another. Furthermore, we choose the difference between the angles of incidence of the collisions of these particles with the boundary walls as our measure for the separation of the trajectories. Eq. (2.1), which was used to express the sensitivity condition, is now expressed by

$$\delta_n = \delta_0 e^{\lambda n}, \quad (5.1)$$

where δ_n refers to the modulus of the difference between the angles of incidence of trajectories after n collisions. As δ_n is calculated *after* n collisions, it is calculated precisely when the particles are on the verge of the $(n + 1)$ th collision. Thus, it follows that δ_0 is the modulus of the difference between the angles of incidence of trajectories at the first collision. Our aim is to find the Lyapunov exponent of the billiard system. We write the necessary code to determine the incident angles at each collision and obtain the set of differences in incident angles between two typical trajectories that started arbitrarily close to each other. In Fig. 5, we plot $\ln(\delta_n/\delta_0)$ against collision points n for two of these typical trajectories. The Lyapunov exponent is the slope of the unsaturated part of the graph. To compute the average Lyapunov exponent, we calculate λ s with many different initial conditions and then take the average. This is done to minimize dependence on initial conditions.

A point in the phase space of a billiard system is considered hyperbolic if its Lyapunov exponent is non-zero. The entire billiard system is referred to as a hyperbolic billiard when the probability of a non-hyperbolic point in the phase space approaches zero. In other words, almost all the points in the phase space of a hyperbolic system are hyperbolic. Because of the presence of multiple flat walls on which the particle can repeatedly bounce off of without encountering a dispersing wall, the Sinai and Superman billiards are non-hyperbolic. The cardioid billiard, on the other hand, is made entirely of dispersing walls and thus, it is a hyperbolic billiard.

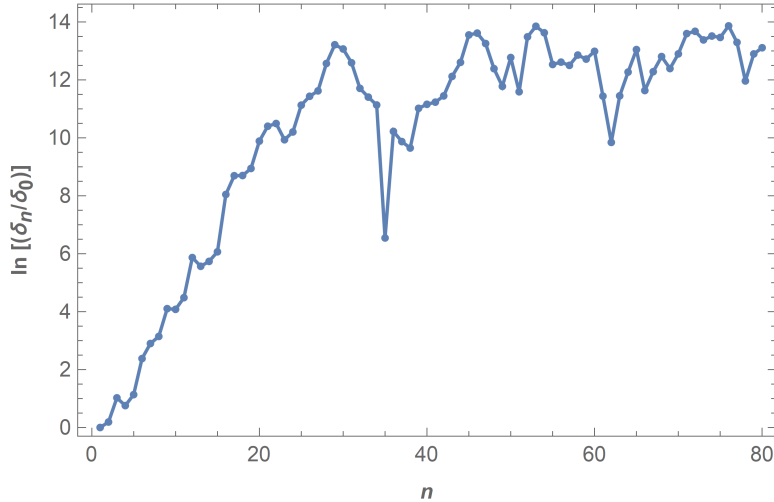


Figure 5: Saturation of Lyapunov exponent for a cos-billiard for $\varepsilon = 0.5$. For this particular pair of typical trajectories, 80 collisions are taken and saturation starts at around 30 collisions. The Lyapunov exponent corresponds to the gradient of the unsaturated region.

5.2 Classical Lyapunov exponents of the three billiards

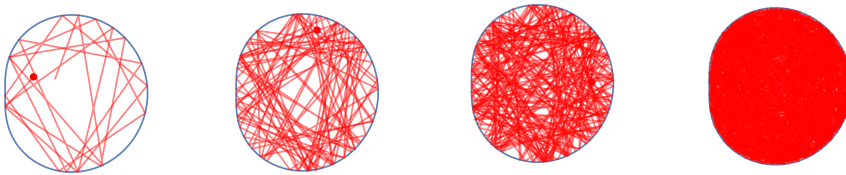


Figure 6: Growth of a typical trajectory inside a cos-billiard for $\varepsilon = 0.5$.

We will employ the numerical method described above to calculate the classical Lyapunov exponents of the Sinai, cardioid, and diamond billiards. However, to compute the exponents, we have to obtain typical trajectories. In numerical simulations, one generates a trajectory of the system, usually by selecting an initial point X_0 randomly. We call these types of trajectories *typical* trajectories. To obtain the particle's trajectory, we numerically solve Newton's equations with elastic reflection condition as boundary conditions. In Fig. 6, we show the growth of a typical trajectory of a particle inside a cos-billiard over a period.

In Fig. 7a, we display, for the Sinai billiard, the typical trajectories (coloured red and blue) of two point particles that start from two extremely close points, $A(1.3, 0.6)$ and $A'(1.3 + 10^{-10}, 0.6 + 10^{-10})$, with very similar velocity components. After just a few collisions, the particles become separated.

Fig. 7b illustrates the growth rate of trajectory separation for the trajectories shown in Fig. 7a as a function of the number of collisions, denoted by n . In this

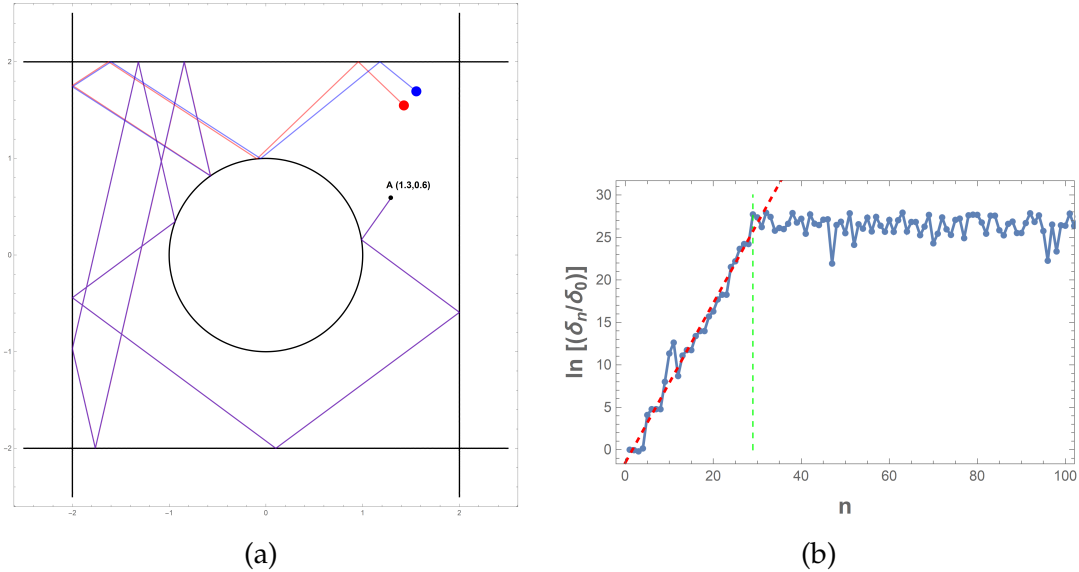


Figure 7: (a) The trajectories of two particles in the Sinai enclosure starting from initial points very close to one another. (b) The growth rate of separation between the trajectories in (a), with respect to number of collisions, n . The dashed green line indicates the saturation point at $n = 29$, while the dashed red line represents the best fit for the unsaturated region. The slope of this red line corresponds to the Lyapunov exponent for this specific pair of trajectories.

case, we have considered approximately 100 collisions, and the saturation point occurs at $n = 29$. The Lyapunov exponent is the slope of the unsaturated part, as given by eq. (5.1).

Figs. 8a and 8b depict the growth rate of separation between a particular pair of trajectories that start out very close to one another for the cardioid and diamond billiards, respectively. Here, the saturation point for the cardioid billiard is at $n = 36$, while for the diamond billiard, it is at $n = 33$.

For each of our billiards, we generated 2000 random initial conditions and from them, generated 2000 pairs of trajectories, each pair consisting of two particles that start out very close to one another. We then calculated 2000 Lyapunov exponents from these pairs of trajectories using the method described above. Finally, we took the average of all the Lyapunov exponents obtained for each particular billiard to arrive at our final value of the *classical* Lyapunov exponent, λ_{cl} , for each billiard. Note that in this computation of the Lyapunov exponent we do not use the distance between collisions. The justification for not using the distance between collisions is given by Appendix B.

However, later in the paper when we compute the quantum Lyapunov exponent we utilize the average distance between consecutive collisions of the classical trajectories as a unit in order to facilitate comparison of the quantum Lyapunov

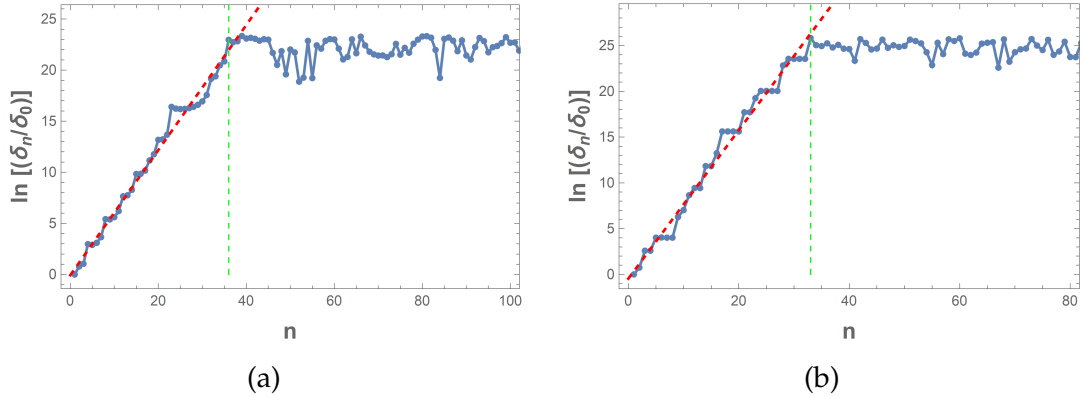


Figure 8: Growth rate of separation between two trajectories that start out extremely close to one another for the (a) cardioid and (b) diamond billiard systems.

exponent with the average classical Lyapunov exponent. We calculated the average distance between two consecutive collision points for the unsaturated part, denoted by d_{avg} for each typical trajectory and then averaged it across the 2000 trajectories. In our calculations, the area of the billiard was consistently kept at 1. Therefore, the average distance between two collisions is calculated for billiards with an area of 1. In Table 1 we list the average distance between consecutive collisions and the classical Lyapunov exponents of our selected billiards.

Billiard	λ_{cl}	d_{avg} for $A = 1$
Sinai	0.8048	0.4817
Cardioid	0.6649	0.8787
Diamond	0.6860	0.7805

Table 1: Average classical Lyapunov exponents λ_{cl} and average distance between consecutive collisions d_{avg} for the Sinai, cardioid, and diamond billiards.

6 Numerical calculation of OTOCs

6.1 OTOCs and Wavefunctions

To compute the OTOCs of billiards we first need to find the eigenvalues of the Hamiltonian operators of the billiards as was described in Subsection 3.1. The Hamiltonian of a billiard is given by

$$H = -\frac{\partial^2}{\partial x^2} - \frac{\partial^2}{\partial y^2} + V_{\text{bill}}(x, y), \quad V_{\text{bill}}(x, y) = \begin{cases} 0, & (x, y) \in \Omega \\ \infty, & \text{elsewhere} \end{cases} \quad (6.1)$$

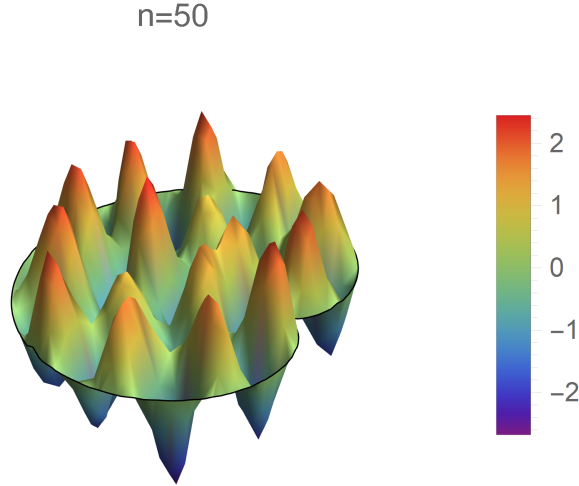


Figure 9: A three-dimensional plot of the cardioid eigenfunction for $n = 50$. The elevation corresponds to the value of the wave function at each point.

where Ω is the region inside the billiard. In Fig. 9, we show a typical wavefunction for the cardioid billiard, ψ_{50} , numerically generated by Mathematica.

We follow the same procedure as with the stadium billiard [9] to calculate the x -matrix elements as

$$x_{nm} = \int_{\Omega} dx dy \psi_n x \psi_m. \quad (6.2)$$

We then calculate the microcanonical OTOCs by substituting the position matrix elements x_{nm} and energy eigenvalues E_n into Eq. (3.7) to obtain $b_{nm}(t)$, which we then use in Eq. (3.3) to calculate the microcanonical OTOCs $c_n(t)$ for each energy level n . Taking the thermal average of $c_n(t)$ using Eq. (3.2), we obtain the thermal OTOCs. Since numerical calculations require truncation of the summations in Eqs. (3.7), (3.3), and (3.2), we must choose a sufficiently large truncation cut-off. We chose to truncate the sums to $I_{\text{trunc}} = 800$ and we show in Appendix A that this truncation value is large enough so that our results remain sufficiently accurate. We show the log plots of the thermal OTOCs of our selected billiards in Fig. 10.

There is a noticeable initial growth in the thermal OTOCs of our selected billiards at short times. These graphs are similar to Fig. 1, where we presented a schematic diagram of the growth of the thermal OTOCs. At later times, the OTOCs stabilize and oscillate around a constant value.

However, at very low temperatures, there is no significant growth in the thermal OTOCs for the diamond and cardioid billiards, and for the cardioid billiard, we observe large oscillations. This behaviour is also observed in the case of low mode microcanonical OTOCs. The reason for this lies in Eq. (3.2), where the Boltzmann factor $e^{-\beta E_n}$ suppresses the contribution from high modes at low temper-

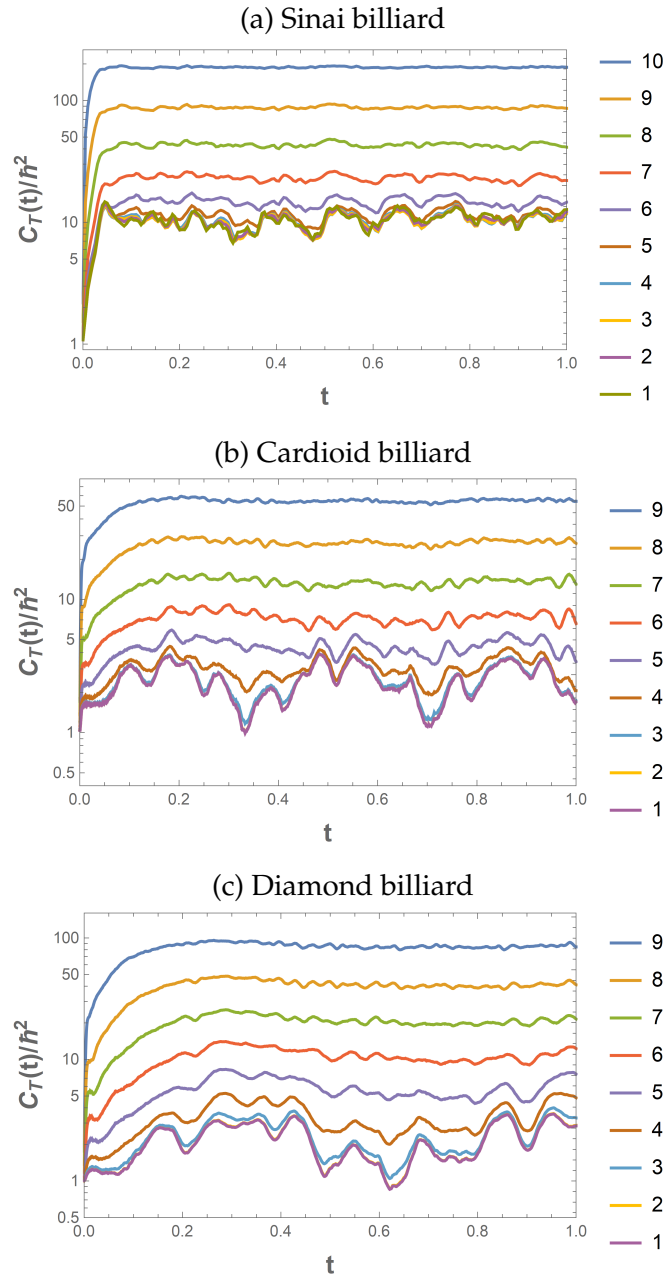


Figure 10: Log plots of thermal OTOCs for (a) Sinai billiard, (b) cardioid billiard, (c) diamond billiard. The corresponding temperatures are given to the right of the graphs, expressed on a log base 2 scale.

atures. Conversely, at higher temperatures, the Boltzmann weight does not suppress the high modes, leading to an increased number of modes contributing to the thermal OTOCs [27].

Nevertheless, we observe a strict initial growth in the thermal OTOCs of the Sinai billiard even at $T = 2$, despite the suppression of high modes by the Boltzmann factor. This initial growth should also be evident in the microcanonical OTOCs of the same billiard. To verify this, we present the microcanonical OTOCs for the Sinai, as well as the cardioid and diamond billiards in Figure 11.

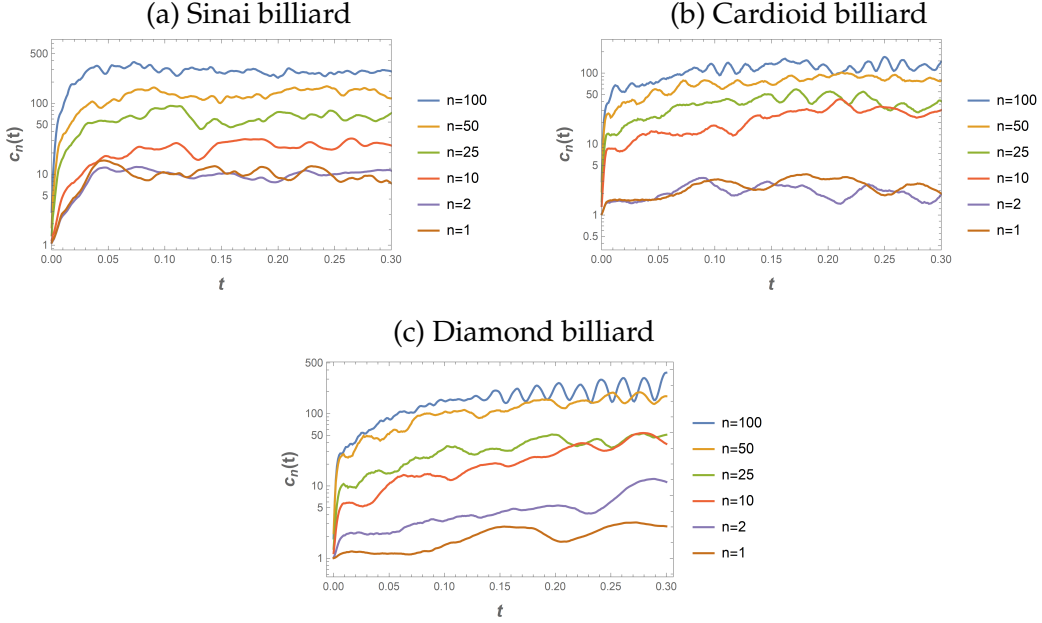
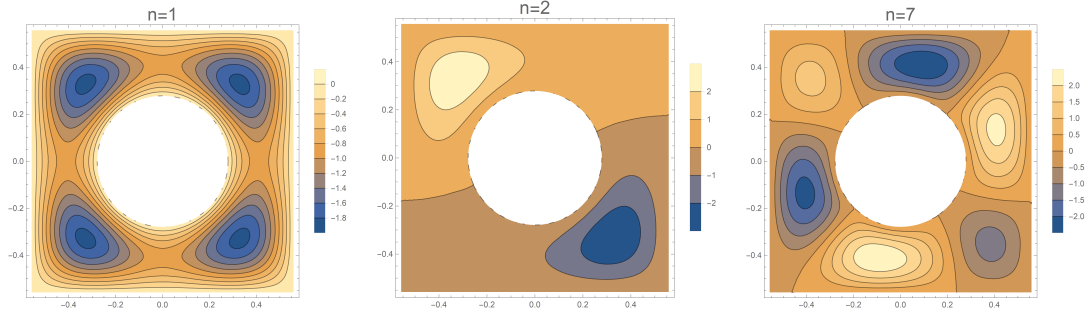


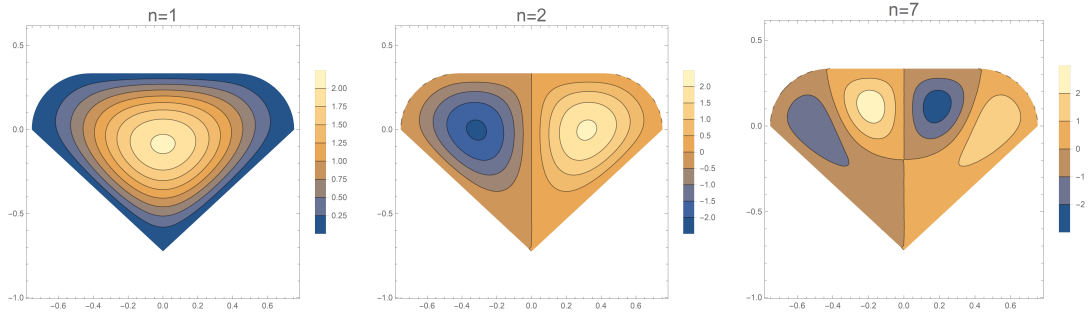
Figure 11: Log plots of microcanonical OTOCs for (a) Sinai billiard, (b) cardioid billiard & (c) diamond billiard.

Indeed, we see that there is initial growth in microcanonical OTOCs of the Sinai billiard for low modes as well. And so, the question arises: why does this initial growth only occur in the case of the Sinai billiard? The answer lies in the shapes of the wavefunctions of these billiard systems with low n -values. In Fig. 12 we can see contour plots of the wavefunctions of the Sinai, cardioid, and diamond billiards for $n = 1, 2, 7$. It is clear from the contour plots that only the Sinai $n = 1$ wave function consists of multiple peaks and troughs, whereas the other $n = 1$ wavefunctions consist of only one peak (or trough). This means that the typical scale (characteristic length scale over which the probability density of the wave function changes significantly) is smaller (as a fraction of the total size of the system) in the case of the Sinai billiard, in comparison to the typical scales of the wavefunctions of the other billiard systems for $n = 1$.

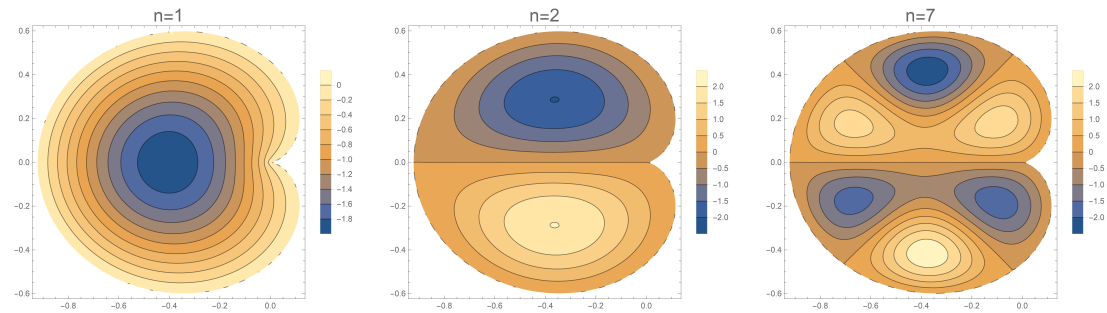
This disparity holds for wavefunctions of these systems corresponding to low



Sinai wavefunctions



Superman wavefunctions



Cardioid wavefunctions

Figure 12: Contour plots of the wavefunctions for the Sinai, diamond and cardioid billiards for $n = 1, 2, 7$.

n . For the diamond, cardioid and stadium billiards, the typical scales of their low n wavefunctions are about the same size as the size of the system. Thus, these wavefunctions do not “feel” the curvature of the walls of their enclosures [9]. However, due to the typical scales of the low n Sinai wavefunctions being significantly smaller than the size of the system, the wavefunctions do experience the curvature of the walls. As a result, the wavefunctions of the Sinai billiard are the only ones out of the four billiard systems to be appreciably affected by the

curvature of the walls at low n . This manifests itself as an initial growth in microcanonical OTOCs of the Sinai billiard corresponding to low n values. It follows that the other three billiard systems do not experience this initial growth in their low-mode microcanonical OTOCs.

6.2 Asymptotic Nature of OTOC at Large Times

The thermal OTOCs for each billiard reach their *saturation* value after a specific time, which is proportional to temperature and consistent with

$$C_s \propto ma^2 k_B T, \quad (6.3)$$

as was observed in [9, 10]. However, estimating the proportionality constant in the semiclassical framework is challenging due to the various possible pairings [28] and the influence of trajectory loops [29, 30]. During the intermediate time window, the OTOC exhibits oscillations with respect to the length parameter, indicating the dynamics of the billiard and periodic-orbit corrections [10].

Although (6.3) was rigorously derived in [10] in the semiclassical limit, [9] was able to derive the same result using dimensional analysis. The argument given in [9] is that the semiclassical regime ends when the wavefunction spreads over the entire system and since $C_T(t)$ has the dimension of \hbar^2 , the only reasonable value of the OTOC is given by (6.3). This shows the power of thinking in terms of specific wave functions and dimensional analysis. Although we know that the exact state of the system is given by the Gibbs state which doesn't evolve over time, useful information is still obtained by thinking in terms of specific wavefunctions which do evolve with time. This is because the OTOC is a time-dependent object and there's much value in thinking of the time dependence in terms of states.

The plots of the OTOCs for large times are given in Fig. 13. It is seen that the oscillations of the OTOCs die down significantly with increasing temperature. The linear growth given by Eq. (6.3) is also manifest in these graphs. The label for the x -axes of these graphs is ℓ/d , which is a proxy for time. This will be explained in more detail in the following section.

7 Quantum Lyapunov Exponents and Thermal OTOCs

When calculating the classical Lyapunov exponent in Section 5, we used collision numbers as the parameter instead of time. By doing so, we essentially replaced the time axis with length in units of average distance between two consecutive collisions. Similarly, we can express the scaled time axis of the thermal OTOCs in units of the average collision distance between two successive collisions. We calculated the average distance between collisions (d_{avg}) for our billiards and presented the values in table 1. This facilitates the comparison between the classical

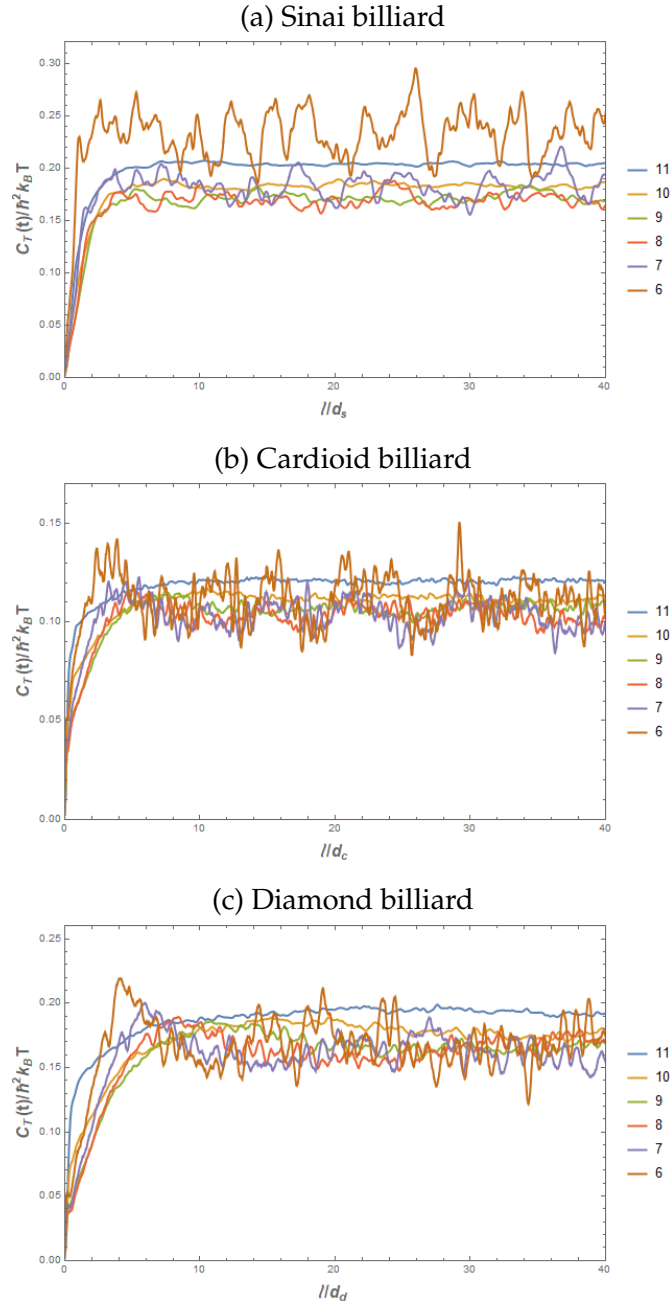


Figure 13: Asymptotic values of OTOCs divided by temperature for the (a) Sinai billiard, (b) cardioid billiard & (c) diamond billiard. Temperatures are expressed on a log base 2 scale. In principle, these graphs have the same information as Fig. 10, but here one can compare fluctuations at different temperatures better. We observe that the oscillations of the asymptotic OTOC die down significantly with increasing temperature. The highest temperatures in these graphs are taken to be much higher to show the persistence of the linear growth of the asymptotic values of OTOCs with temperature.

Lyapunov exponent and the quantum Lyapunov exponent. In this section, we derive the quantum Lyapunov exponents for the three billiards.

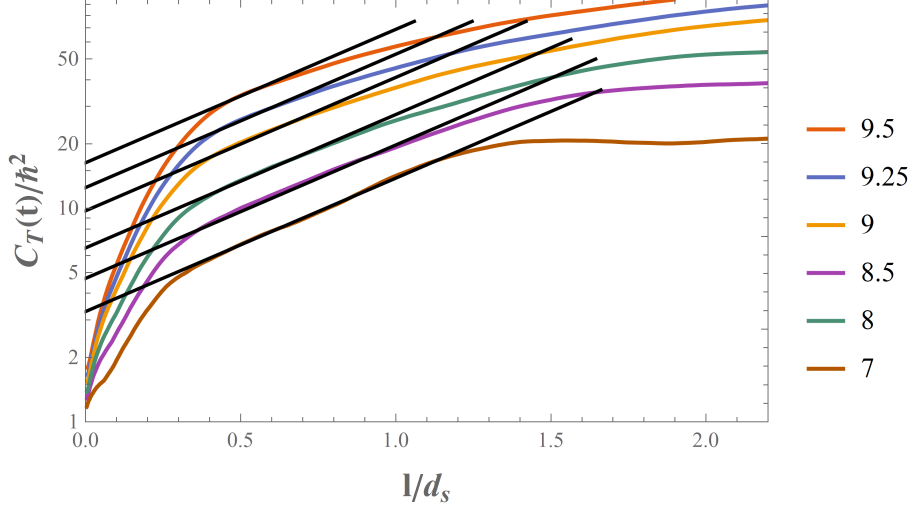


Figure 14: Numerically calculated thermal OTOCs on a logarithmic scale, with respect to the length (scaled time) $\ell = \tilde{v}t$ (in units of d_s), where $\tilde{v} = (\beta m)^{-1/2}$ is the mean-squared x -velocity component, and d_s is the average collision distance calculated in Sec. 5 for the **Sinai billiard**. The temperatures are on a logarithmic scale of base 2. The black straight lines correspond to the exponential growth $a(T)e^{\sqrt{3}\lambda_g\tilde{v}t}$, which accurately fits the data within an intermediate time-window $0.4 \leq \ell/d_s \leq 1.3$.

We exhibit the thermal OTOCs for the Sinai billiard as a function of scaled time in Fig. 14. On the x -axis, we have ℓ/d_s . Here, $\ell = \tilde{v}t$ has the dimension of length but it is essentially time scaled by $\tilde{v} = (k_B T/m)^{1/2}$ which is the mean squared X -component of the velocity. The colour code reflects the temperature, which is expressed in a logarithmic scale of base 2. To achieve a comparable time scale as our classical calculation, the x -axis is expressed in units of the average collision distance, which is $d_{\text{avg}} = d_s = 0.4817$ for the area of the billiard $A = 1$.

In the short time regime, the behaviour of the OTOCs can be divided into two distinct parts. Initially, there is a quadratic increase in the OTOC with respect to time or length, which is characteristic of quantum perturbation theory. This is followed by a rapid growth, leading to a window of exponential increase in the OTOC. The semiclassical approach is valid for the second interval but unsuitable for the initial perturbative or rapid growth periods. This is because they correspond to times much earlier than the time of the first collision with the boundaries when the exponential divergence of classical trajectories has not begun to take place.

To determine the quantum Lyapunov exponent, one first needs to express the

OTOC in the semiclassical regime. It turns out the derivation of the semiclassical expression for the OTOC for systems with low degrees of freedom is a non-trivial task. Based on the path-integral treatment of [15], the authors of [10, 12] derived the following semiclassical expression for the OTOC

$$C_{\text{sc}}(t) = \frac{\beta^2 \hbar^2}{64\pi m^2} \int d\mathbf{p} \exp\left\{-\beta \frac{\mathbf{p}^2}{2m}\right\} (e^{2\lambda t} p_x^2). \quad (7.1)$$

From this, one gets for low-temperature billiards the following expression

$$\frac{C_{LT}(t)}{\hbar^2} \propto \exp\left[\sqrt{3}\lambda_g \tilde{v}t\right]. \quad (7.2)$$

where λ_g is known as the “geometric” Lyapunov exponent. For short time window and low temperatures, the raw exponent Λ that one obtains from the graphs is

$$\Lambda = \sqrt{3}\lambda_g \tilde{v}. \quad (7.3)$$

from which one extracts the geometric Lyapunov exponent.

For the Sinai billiard we have $\lambda_g = 0.83 d_s^{-1}$. In Fig. 14, the solid black lines represent the exponential functions $\mu(T)e^{\sqrt{3}\lambda_g \tilde{v}t}$, which well approximate the OTOCs within the temperature range $2^7 \leq T \leq 2^{9.5}$. As the temperature increases beyond upper limit, the time window of exponential growth starts to shrink until it disappears (more about this below in Subsection 8). Remarkably, although both the value of the L.H.S. of Eq. (7.2) as well as the range of the exponential region vary with temperature, the slope of the curves remains the same. This was also observed in the case of the quarter-stadium billiard in [10].

In classical calculations of the Lyapunov exponent, neither the area of the billiard nor the particle’s velocity plays a role. In Table 1, we denoted the average classical Lyapunov exponent extracted from classical calculations as λ_{cl} . In the quantum calculation, however, the geometric Lyapunov exponent *does* depend on the area of the billiard. Nonetheless, the factor 0.83 in the geometric Lyapunov exponent for the Sinai billiard remains independent of both the area of the billiard and the velocity of the particle. Given that the distance between two collisions is set to one (see, Appendix B) in our classical calculation, we must multiply the geometric Lyapunov exponent obtained from the quantum calculation by the average collision distance:

$$d_{\text{avg}}\lambda_g = \lambda_{\text{qu}}, \quad (7.4)$$

where we have introduced λ_{qu} as the quantum analog of λ_{cl} . Note that this way of expressing the Lyapunov exponent makes it a dimensionless quantity. Should one need the traditional dimensions, one can use Eq. (7.3).

Figure 15 displays the thermal OTOCs for the cardioid and diamond billiards as a function of scaled time. The scaled time (length), denoted as $\ell = \tilde{v}t$, is given in

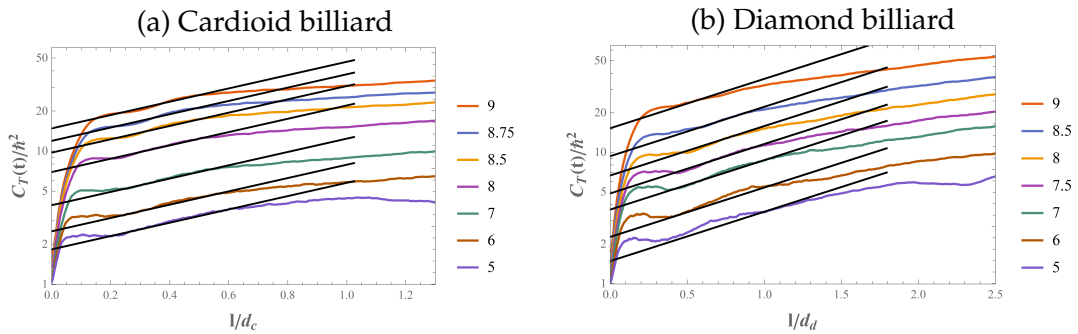


Figure 15: Numerically calculated thermal OTOCs on a logarithmic scale, with respect to the length (scaled time) $\ell = \bar{v}t$ (in units of average collision distance) for (a) cardioid billiard and (b) diamond billiard. The temperatures are on a logarithmic scale with a base of 2. The black straight lines correspond to the exponential growth $a(T)e^{\sqrt{3}\lambda_g\bar{v}t}$, accurately fitting the data within an intermediate time-window of $0.1 \leq \ell/d_c \leq 0.75$ for the cardioid billiard and $0.1 \leq \ell/d_d \leq 1.5$ for the diamond billiard.

units of average collision distances for $A = 1$ and is indicated as d_c for the cardioid billiard and d_d for the diamond billiard. The values of $d_c = 0.8787$ and $d_d = 0.7805$ are taken from Table 1. The range of temperatures where the exponential functions provide the best fit is $2^5 \leq T \leq 2^9$ for both the cardioid and diamond billiard.

The quantum Lyapunov exponent λ_{qu} is extracted in a similar way as for the Sinai billiard by fitting the exponential function to the data. Table 2 compares the classical Lyapunov exponent (λ_{cl}) and the quantum Lyapunov exponent (λ_{qu}) for our selected billiards.

Billiards	λ_{cl}	λ_{qu}
Sinai	0.805	0.83
Cardioid	0.665	0.665
Diamond	0.686	0.5

Table 2: Numerically calculated average geometric classical Lyapunov exponents λ_{cl} and average quantum Lyapunov exponents λ_{qu} extracted from thermal OTOCs for the Sinai, cardioid, and diamond billiards.

Remarkably, we found that the quantum Lyapunov exponent is in excellent agreement to the classical Lyapunov exponent computed in Sec. 5 for the cardioid billiard and the values for the Sinai billiard are also very close. This matching of the classical and quantum exponents are a consequence of Ehrenfest’s theorem and is expected to hold until Ehrenfest time. There is, however, a larger difference

between the values of the calculated quantum and classical Lyapunov exponents in the case of the diamond billiard.

For the thermal OTOCs the window where we expect exponential growth is temperature-dependent. To observe this window of exponential growth more clearly we plot the OTOCs but divided, first by $\exp(\sqrt{3}\lambda_g \ell)$ and then by $\mu(T) \times \exp(\sqrt{3}\lambda_g \ell)$ where $\mu(T)$ is the temperature-dependent prefactor. These plots are shown in Figs. 16a and 16b. Both figures contain the same information, but the first figure, shows the width of the exponential region of each individual OTOC more clearly, whereas the second plot is better for comparison between different curves. In these plots we see that as the temperature increases, the width of the exponential regime decreases until it finally disappears.

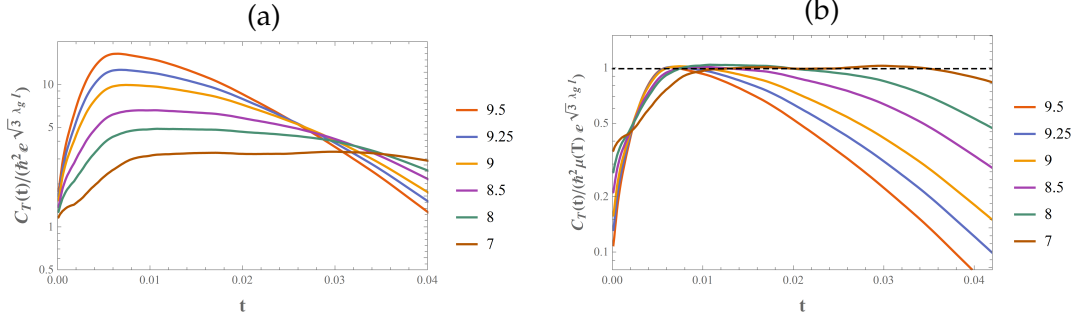


Figure 16: Numerically calculated thermal OTOCs of the **Sinai billiard** on a logarithmic scale: (a) scaled by $\exp(\sqrt{3}\lambda_g \ell)$, and (b) scaled by $\mu(T) \exp(\sqrt{3}\lambda_g \ell)$ as a function of time t . The temperatures are represented on a logarithmic scale with a base of 2.

The analogous plots of the thermal OTOCs for cardioid and diamond billiards are given in Fig.17. The results are consistent with our earlier findings: as the temperature increases, the fit to the exponential function gradually worsens.

8 Temperature Dependence of Ehrenfest Times

Dimensional Analytic Estimates

In the semiclassical regime, the growth of the OTOC is controlled by the exponent $\Lambda = \sqrt{3}\lambda_g \tilde{v}$ (Eq. 7.3). Because of the presence of the rms velocity \tilde{v} , this exponent is proportional to \sqrt{T} . As observed in [10] and also by our data, in the region where one finds exponential growth, the value of Λ is consistent with the proposed bound on the growth rate of OTOCs given by $\Lambda \leq 4\pi k_B T / \hbar$ [6].

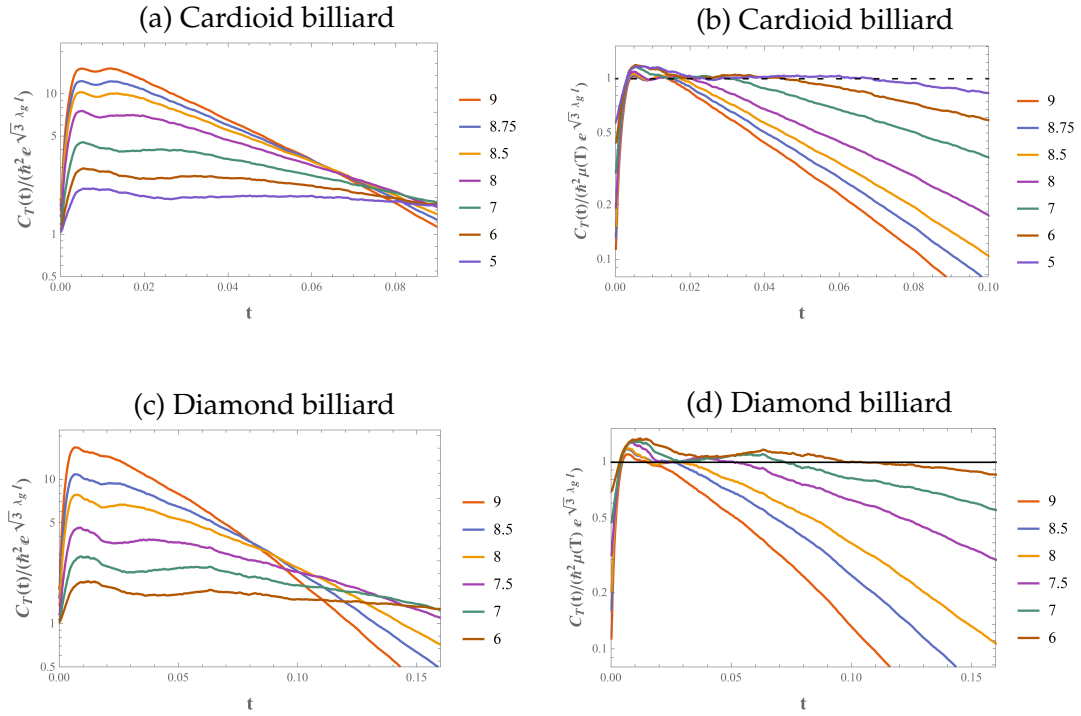


Figure 17: Numerically calculated thermal OTOCs of cardioid on a logarithmic scale: (a) scaled by $\exp(\sqrt{3}\lambda_g\ell)$, and (b) scaled by $\mu(T)\exp(\sqrt{3}\lambda_g\ell)$ as a function of time t . Numerically calculated thermal OTOCs of the diamond billiard on a logarithmic scale: (c) scaled by $\exp(\sqrt{3}\lambda_g\ell)$, and (d) scaled by $\mu(T)\exp(\sqrt{3}\lambda_g\ell)$ as a function of time t . As in the case of the Sinai billiard, the temperatures are expressed on a \log_2 scale.

However, the region of exponential growth is related to the temperature. Since the end of the exponential growth with respect to time marks the transition from the semiclassical regime to the fully quantum regime, we can mark the transition point as the Ehrenfest time t_E . We want to understand how the Ehrenfest time depends on the temperature T .

The naive intuition is that the faster a wavepacket moves the quicker it will disperse and spread over the whole billiard. Since we are dealing with a system at a specific temperature, it picks out the rms velocity $\tilde{v} \sim \sqrt{T}$. Thus our naive, zeroth-order expectation is that the Ehrenfest time should have the form

$$t_E \sim \frac{1}{\sqrt{T}}. \quad (8.1)$$

This is borne out if we consider the evolution of a Gaussian wavepacket as was done in [9]. The reflection of the wave function at the billiard walls will deform its

shape, but to the lowest order of approximation we can still consider it to be localized (this corresponds to the validity of the particle approximation). As is well known from elementary quantum mechanics [31], the uncertainty of a Gaussian wavepacket evolves with time according to

$$\Delta x(t) = \Delta x_0 \sqrt{1 + \left(\frac{t}{\tau}\right)^2} \quad (8.2)$$

where $\Delta x_0 \equiv \Delta x(0)$ and $\tau \equiv 2m\Delta x_0^2/\hbar$ is the time scale after which the width of the Gaussian changes significantly. From the thermal de Broglie wavelength for a quantum particle we set

$$\Delta x_0 = \sqrt{\frac{2\pi\hbar^2}{mk_B T}}. \quad (8.3)$$

The Gaussian starts to change shape significantly when $t \simeq \tau$ and so we can expect t_E to be given by (switching to our units)

$$t_E \sim \frac{L}{\sqrt{T}} \quad (8.4)$$

where $L = \Delta x(t_E)$ is the typical system size.

One might object to this dimensional analysis argument saying that the uncertainty of the thermal state is time-independent and thus its uncertainty has no “evolution.” But, observe that one can decompose a thermal state in a basis of (over-complete) squeezed states and track their evolution in time. While it is true that the Gibbs state is invariant under time evolution, it is the nature of OTOC to introduce dynamics in this scenario. For the evolution of the OTOC, one expects that it would be dominated by the Gaussian with the length scale set by the temperature of the system. One can miss the semiclassical growth of the OTOC (see [13], for example) that was found in [10] if one ignores the “dynamics” in the thermal state.

There is another, *independent* argument as to why the Ehrenfest time for quantum billiards should have $1/\sqrt{T}$ dependence. We can interpret the commutator $[x(t), p]$ as representing the failure in the simultaneous precise measurement of the position of the particle at time t after an initial measurement of its momentum p at $t = 0$ and vice versa³. Thus one can make the following crude approximation

$$\langle [x(t), p]^2 \rangle \simeq (\Delta x(t)\Delta p_0)^2 \quad (8.5)$$

³Note that unitarity means that we can reverse evolve our state from time t to 0. What we are proposing here is reminiscent of the Loschmidt echo.

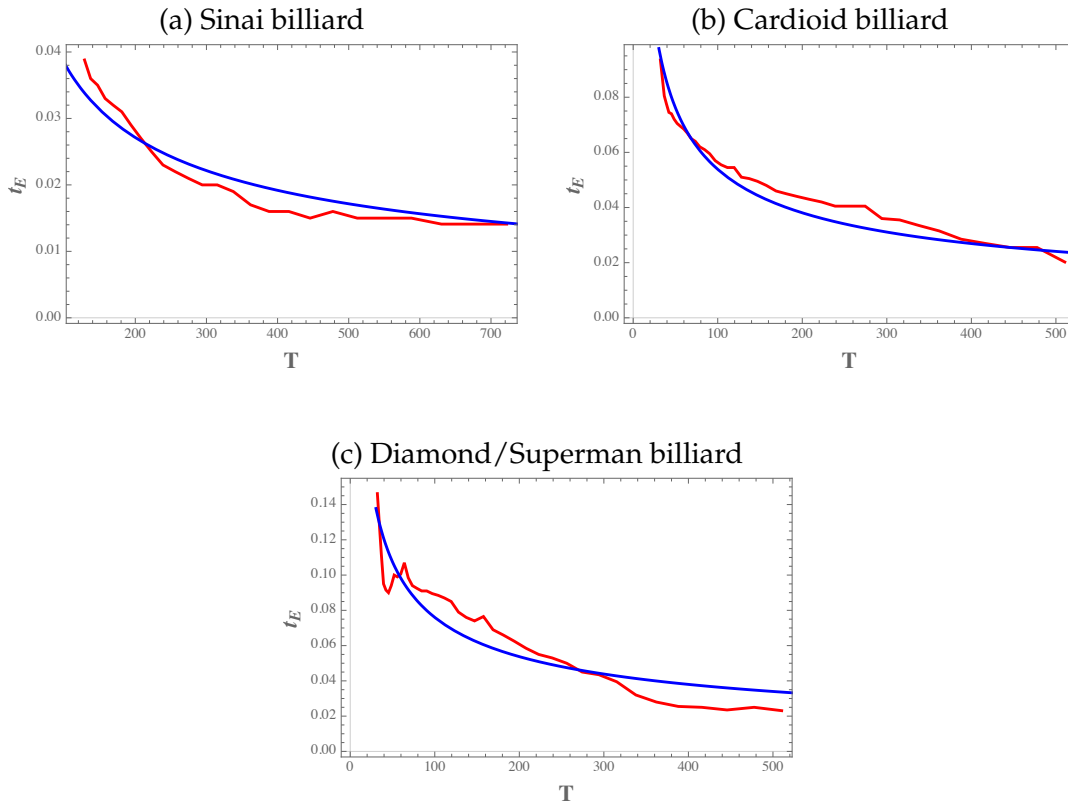


Figure 18: The dependence of the **Ehrenfest time** t_E on the **temperature** T for each billiard. The red curves represent the data obtained by numerics while the blue curve is the fitted curve. The fitting was done with the function $t_E = c/\sqrt{T}$.

One can use (8.2), (8.3), and $\Delta x_0 \Delta p_0 \simeq \hbar$ on the right-hand side and the observation that $C(t \rightarrow \infty) \sim T$ from (6.3) on the left-hand side, to obtain the *same* temperature dependence $t_E \sim 1/\sqrt{T}$.

Note that, in this second argument, the asymptotic dependence of the OTOC on temperature, as given by (6.3) (and verified by our data), is a *new* input which makes it independent from the previous argument.

In Fig. 18, we see a general agreement between the data and our approximation given by $t_E \simeq c/\sqrt{T}$, with $c(\text{Sinai}) = 0.383614$, $c(\text{cardioid}) = 0.538536$, and $c(\text{Superman}) = 0.759939$. We see that these numbers are of the same order of magnitude as the length scale of the billiards.

9 Discussion

The OTOC represents a novel and interesting approach to studying quantum chaos. Although mainly used to study many-body systems, following [7, 9, 10, 13]

we found that it is also a good tool for studying the quantum chaos of systems with a small number of degrees of freedom, namely chaotic billiards. In this paper, we were mainly concerned with the quantum Lyapunov exponents and the semiclassical regime of three quantum billiards which are known to be chaotic classically. We exclude a detailed examination of the stadium billiard as it has been examined extensively in recent papers using OTOCs as the primary tool [9, 10, 13].

We found that the agreement between the classical and quantum exponents is excellent for the Sinai and cardioid billiards but for the diamond billiard it is not as good (see Table 2). It is also worth noting that, try as we might, our computation of the classical Lyapunov exponent for the diamond/Superman could not reproduce the results of [25]. Interestingly, it is their *classical* value that is close to the *quantum* Lyapunov exponent that we computed. Since we used the same code and technique to compute the Lyapunovs of all the billiards in this paper, we cannot dismiss the result of the diamond/Superman billiard as a fluke. This is a discrepancy that needs to be looked into more carefully.

Even in such simple systems, we found interesting phenomena in terms of the growth of OTOC of the Sinai billiard at low temperature. We traced this anomalous behaviour to the symmetry of the ground state of the wave function of the Sinai billiard which reflects the geometry of the billiard in contrast to the low-energy states of the other billiards. This observation provides a counterexample to the point of view that the microcanonical OTOCs for low n may not see the curvature of the billiard because of the typical scales of the wave function for small energy being of the same size as the system [9]. We also see a lot more structure in the long-time OTOC of the Sinai billiard at low temperatures compared to the other billiards at low temperatures (Fig. 13).

As argued in [11], the OTOC measures the ballistic growth of Heisenberg operators. Thus for systems of finite sizes, there comes a time when this growth is saturated. The time at which this happens is the scrambling time. Here we prefer to call it Ehrenfest time t_E , as it is the time at which the wave function of a quantum particle has spread out over the whole system so that one can no longer expect the semiclassical regime (*i.e.*, Ehrenfest's theorem) to hold. Using, admittedly, very rough dimensional analysis we presented *two* logically independent arguments as to why the Ehrenfest time t_E for the three billiards presented in this paper should depend on temperature as $1/\sqrt{T}$. We have also presented numerical data to back up this claim. This is the zeroth order approximation and the data of the Ehrenfest time's dependence on temperature has a lot of structure in it. It would be an interesting exercise to look at this relationship in greater detail in a future publication.

Acknowledgments

We are very grateful to the authors of [10] for insightful and helpful correspondence.

A Assessment of the error resulting from level truncation

At various points during our calculations of OTOCs, namely Eqs. (3.7), (3.3), and (3.2), we encounter infinite sums. As we evaluate these sums via numerical calculations, the infinite sums in these equations must be truncated to a certain cut-off value, I_{trunc} . In this segment, we determine the effect of taking different values of I_{trunc} on the OTOCs with the aim of ascertaining a suitable cut-off value. We shall focus on the Sinai billiard and compute the microcanonical OTOC for $n = 100$ for various truncation values I_{trunc} . The microcanonical OTOCs for $I_{\text{trunc}} = 100, 150, 200, 400, 600, 800$ are shown below.

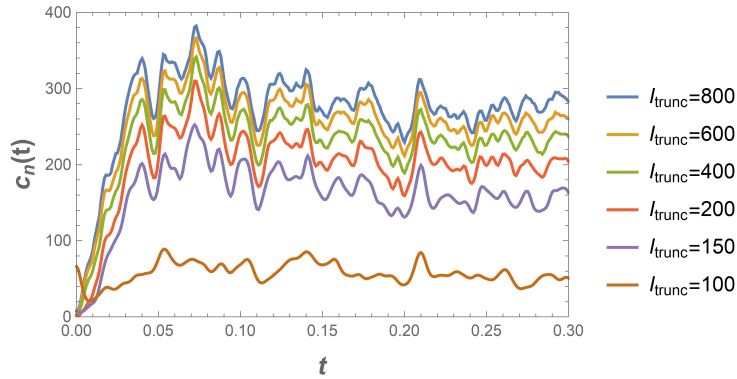


Figure 19: Microcanonical OTOCs of the Sinai billiard corresponding to $n = 100$ for $I_{\text{trunc}} = 100, 150, 200, 400, 600, 800$.

As we can see, the microcanonical OTOCs for $n = 100$ converge fairly well as the value of I_{trunc} is increased from 100 to 800. We found similar convergences for microcanonical OTOCs with $n < 100$. As n increases above 100, the corresponding microcanonical OTOCs do not contribute to the thermal OTOCs to a significant extent. This is because the $\exp\left(\frac{-E_n}{T}\right)$ term in Eqn. (3.2) suppresses the contributions of microcanonical OTOCs corresponding to large n . As a result, the microcanonical OTOCs for $n \leq 100$ converging well at our truncation value I_{trunc} is sufficient for our purposes. Therefore, we picked $I_{\text{trunc}} = 800$ for our calculations of the Sinai OTOCs. Furthermore, we found, through similar analyses, that $I_{\text{trunc}} = 800$ was a suitable truncation value for the cardioid and diamond billiard systems as well. Thus, we truncated the infinite sums to $I_{\text{trunc}} = 800$ during the calculations of the OTOCs of those systems as well.

B Averaging Collision Distance to Scale Length Parameters

We plot a graph of a random trajectory in a classical billiard in Fig. 20a, where the slope of the unsaturated part represents the Lyapunov exponent. The x -axis denotes the collision number n . Although the *actual* distances between n_1 and n_2 , and between n_2 and n_3 , differ, we consider them equal and set the separation to 1 when plotting the points.

In Fig. 20b, we plot a graph where we recorded the exact distance between each pair of collisions, compiled a list, and plotted the points accordingly. This accurately represents the position of each point on the y -axis based on the distance traveled from the initial point. However, we scaled the x -axis by dividing it by the average collision distance up to the unsaturated part for this specific trajectory. This adjustment is necessary because the previous graph has a unit distance between n_1 and n_2 , n_2 and n_3 , and so forth. To achieve comparable scaling on the x -axis in the second graph, we needed to divide it by the average collision distance.

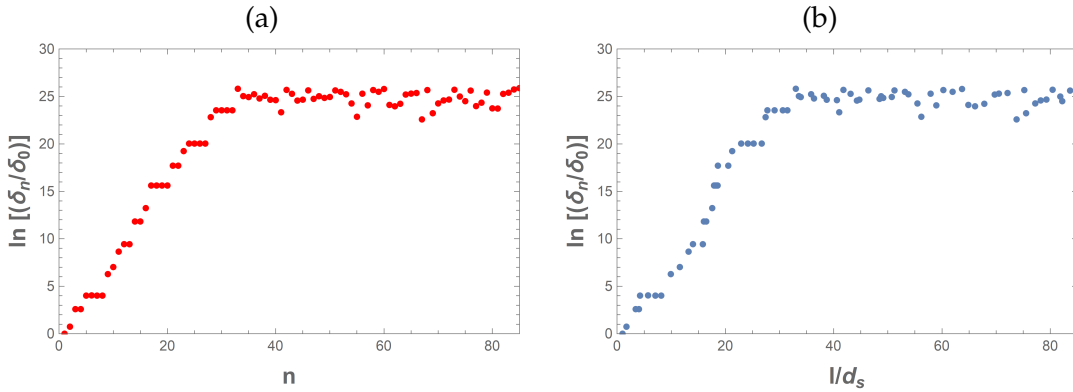


Figure 20: The growth rate of separation between two trajectories inside the Sinai billiard that start out extremely close to one another is depicted as follows: (a) with respect to collision number n , and (b) with respect to length scaled with the average distance between two consecutive collisions.

Now, in Fig. 21, we plot the graphs together, observing that both follow a narrow lane and exhibit very similar growth rates. This observation has motivated the use of the average collision distance as a unit for OTOCs when comparing the growth rates of the OTOCs to the classical growth rates of separation. As the number of random initial points increases, the average Lyapunov exponent appears to converge to a more accurate value.

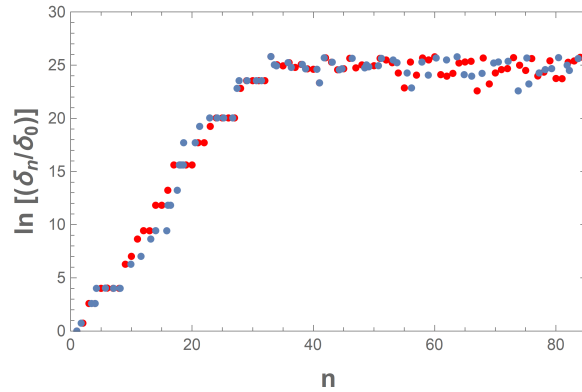


Figure 21: Fig. 20a and Fig. 20b plotted together.

References

- [1] A.I. Larkin and Y.N. Ovchinnikov, *Quasiclassical method in the theory of superconductivity*, *Soviet Physics JETP* **28** (1969) 1200.
- [2] S.H. Shenker and D. Stanford, *Black holes and the butterfly effect*, *Journal of High Energy Physics* **2014** (2014) .
- [3] S.H. Shenker and D. Stanford, *Multiple shocks*, *Journal of High Energy Physics* **2014** (2014) .
- [4] A. Kitaev, *Hidden correlations in the hawking radiation and thermal noise*, talk given at *Fundamental Physics Prize Symposium* (2014) .
- [5] S.H. Shenker and D. Stanford, *Stringy effects in scrambling*, 2015.
- [6] J. Maldacena, S.H. Shenker and D. Stanford, *A bound on chaos*, *Journal of High Energy Physics* **2016** (2016) .
- [7] E.B. Rozenbaum, S. Ganeshan and V. Galitski, *Lyapunov exponent and out-of-time-ordered correlator's growth rate in a chaotic system*, *Physical Review Letters* **118** (2017) .
- [8] H. Gharibyan, M. Hanada, B. Swingle and M. Tezuka, *Quantum lyapunov spectrum*, *Journal of High Energy Physics* **2019** (2019) .
- [9] K. Hashimoto, K. Murata and R. Yoshii, *Out-of-time-order correlators in quantum mechanics*, *Journal of High Energy Physics* **2017** (2017) .
- [10] R.A. Jalabert, I. García-Mata and D.A. Wisniacki, *Semiclassical theory of out-of-time-order correlators for low-dimensional classically chaotic systems*, *Physical Review E* **98** (2018) .
- [11] B. Swingle, *Unscrambling the physics of out-of-time-order correlators*, *Nature Physics* **14** (2018) 988.
- [12] I. García-Mata, R.A. Jalabert and D.A. Wisniacki, *Out-of-time-order correlators and quantum chaos*, *Scholarpedia* **18** (2023) 55237 [2209.07965].

- [13] E.B. Rozenbaum, S. Ganeshan and V. Galitski, *Universal level statistics of the out-of-time-ordered operator*, *Physical Review B* **100** (2019) .
- [14] I. García-Mata, M. Saraceno, R.A. Jalabert, A.J. Roncaglia and D.A. Wisniacki, *Chaos signatures in the short and long time behavior of the out-of-time ordered correlator*, *Phys. Rev. Lett.* **121** (2018) 210601.
- [15] M. Gutzwiller, *The semi-classical quantization of chaotic hamiltonian systems*, in *Chaos and Quantum Physics*, Z.-J. Giannoni, Voros, ed., pp. 201–250, North Holland, Amsterdam (1991).
- [16] D. Marković and M. Čubrović, *Detecting few-body quantum chaos: out-of-time ordered correlators at saturation*, *Journal of High Energy Physics* **2022** (2022) .
- [17] N. Anand, G. Styliaris, M. Kumari and P. Zanardi, *Quantum coherence as a signature of chaos*, *Phys. Rev. Res.* **3** (2021) 023214.
- [18] Y.G. Sinai, *Dynamical systems with elastic reflections*, *Russian Mathematical Surveys* **25** (1970) 137.
- [19] L. Zarfaty, A. Peletskyi, E. Barkai and S. Denisov, *Infinite horizon billiards: Transport at the border between gauss and lévy universality classes*, *Phys. Rev. E* **100** (2019) 042140.
- [20] Y.G. Sinai, *Dynamical systems with elastic reflections*, *Russian Mathematical Surveys* **25** (1970) 137.
- [21] E.G. Altmann, *Intermittent chaos in Hamiltonian dynamical systems*, Ph.D. thesis, Verlag nicht ermittelbar, 2007.
- [22] M.P. Wojtkowski, *Principles for the design of billiards with nonvanishing lyapunov exponents*, *Communications in Mathematical Physics* **105** (1986) 391.
- [23] D. Szász, *On the K-property of some planar hyperbolic billiards*, *Communications in Mathematical Physics* **145** (1992) 595.
- [24] R. Markarian, *New ergodic billiards: exact results*, *Nonlinearity* **6** (1993) 819.
- [25] R. Salazar, G. Téllez, D. Jaramillo and D.L. González, *Classical and quantum chaos in the diamond shaped billiard*, 2012.
- [26] D.J. R. Salazar, G. Tellez and D. Gonzalez, *Chaos in the diamond-shaped billiard with rounded crown*, *Rev. Acad. Colomb. Cienc. Ex. Fis. Nat* **39** (2015) .
- [27] T. Akutagawa, K. Hashimoto, T. Sasaki and R. Watanabe, *Out-of-time-order correlator in coupled harmonic oscillators*, *Journal of High Energy Physics* **2020** (2020) .
- [28] M. Gutiérrez and A. Goussev, *Long-time saturation of the loschmidt echo in quantum chaotic billiards*, *Phys. Rev. E* **79** (2009) 046211.
- [29] M. Sieber and K. Richter, *Correlations between periodic orbits and their role in spectral statistics*, *Physica Scripta* **2001** (2001) .
- [30] B. Gutkin, D. Waltner, M. Gutiérrez, J. Kuipers and K. Richter, *Quantum corrections to fidelity decay in chaotic systems*, *Phys. Rev. E* **81** (2010) 036222.

[31] J.L. Powell and B. Crasemann, *Quantum Mechanics*, Addison-Wesley (1961).